Correlation of Capacity Fading Processes and Electrochemical Impedance Spectra in Lithium/Sulfur Cells

Sebastian Risse[1,*], Natalia A. Cañas[2], Norbert Wagner[2], Eneli Härk[1,3], Matthias Ballauff[1] and K. Andreas Friedrich[2,4]

[1]Institute for Soft Matter and Functional Materials, Helmholtz Zentrum Berlin, Hahn-Meitner Platz 1, 14109 Berlin, Germany

[2]Institute of Engineering Thermodynamics, German Aerospace Center, Pfaffenwaldring 38-40, 70569 Stuttgart, Germany

[3]Institute of Chemistry, University of Tartu, Ravila 14a, 50411 Tartu, Estonia

[4]Institute of Energy Storage, University of Stuttgart, Stuttgart, 70550, Germany

Abstract

The capacity fading of lithium/sulfur (Li/S) cells is one major challenge that has to be overcome for a successful commercialization of this electrochemical storage system. Therefore it is essential to detect the major fading mechanisms for further improvements of this system. In this work, the processes leading to fading are analyzed in terms of a linear four state model and correlated to the distribution of relaxation times calculated with a modified Levenberg-Marquardt algorithm. Additionally, the Warburg impedance and the solution resistance are also obtained by the same algorithm. The detailed analysis of intermediate states during the first cycle gives the distinction between relaxation processes at the sulfur cathode and at the lithium anode. The influence of the polysulfides on the impedance parameters was evaluated using symmetric cells; this yields a good correlation with the results obtained from the first discharge/charge experiment. A fast and a slow capacity fading process are observed for the charge and the discharge during 50 cycles. The fast fading process can be assigned to Faradaic reactions at the lithium anode.

Keywords: lithium sulfur battery, capacity fading, electrochemical impedance spectroscopy, Levenberg-Marquardt algorithm, distribution of relaxation times

Introduction

Lithium sulfur (Li/S) batteries are a promising candidate for the due to their high theoretical gravimetric energy density of 2650 Wh/kg_{sulfur} [1–3]. The low cost, low environmental impact, and their abundant raw materials are further important advantages that have led to intense research on this system [4]. A major drawback is the capacity fading with increasing number of cycles [5–7]. The reasons for this decrease of capacity can be found for instances in the loss of active sulfur species at the cathode (shuttle effect) [8], the drying out of the electrochemical cell by solvent decomposition [9], the formation of electrically disconnected lithium [10] and the precipitation of insoluble species at the anode that occupy active reaction sites [11]. Many studies have been published that aim at deeper insights into the processes that occur in this complex electrochemical system during charge and discharge [12–17]. An empirical model was recently presented [18] that analyses the fading curves in terms of a linear four state model.

The formation of the dynamic and complex surface layer between the liquid electrolyte and each of both solid electrodes is central for the cycling stability of the cell [19–21]. This solid electrolyte interphase (SEI) layer can be regarded as a mediator that controls intercalation, diffusion and the charge transfer reaction of the cations and anions. The resulting characteristic Faradaic currents at each electrode give information about the oxidation and reduction processes in an electrochemical cell. A powerful method to analyze these processes is electrochemical impedance spectroscopy (EIS). It can also be applied to many other systems like fuel cells, catalysts, electrochemical capacitors *etc.* [21–24] and it is facile to perform. It gives access to characteristics of electrochemical cells like the Warburg impedance (diffusion of ions), double layer capacity, charge transfer resistance and electrolyte resistance. Also, the various Faradaic reaction processes that occur at the SEI between liquid electrolyte and solid electrode can be investigated with this method [20,25–28]. The EIS data obtained leads to information that is often hard to interpret [29]. In particular, the decomposition of all these processes and the proper determination of all relaxation processes are difficult to achieve. The choice of several resistance-capacitance elements or constant phase elements may lead to overfitting the data [30,31].

The analysis of Li/S cells with EIS is the subject of intense research. In the work by Yuan *et al.* [32] and Cañas *et al.* [23] EIS spectra were recorded at intermediate states during the first charge and discharge that could be linked to processes in the electrolyte and at the sulfur cathode. While Deng *et al.* [5] highlight the important influence of agglomerates at the sulfur cathode on the capacity fading process, Xiong *et al.* [33] emphasize the important role of the lithium anode and suggested a multi-layer system on this metal electrode. Indication of layered structures on metallic lithium obtained by EIS was also published by Aurbach and Zabane [34,35]. All these publications make use of Nyquist plots and fittings to equivalent circuit containing constant phase or resistance-capacitance elements to investigate the charge transfer processes.

Another way to analyze the Faradaic reaction processes in battery systems is the distribution of relaxation times (DRT) method [24,25,36,37]. The application of this method clearly eases the determination and distinction of charge transfer processes. However, the determination of such DRT-functions inevitably leads to an ill-posed problem that can only be numerically solved.

In this work, we apply the Levenberg-Marquardt algorithm (LMA) that is a standard technique used to solve nonlinear least square problems [38]. The equivalent circuit model used consists of only four elements connected in series that represent the major properties of a battery like the charge transfers at both electrodes, the solution resistance, the Warburg resistance (diffusion), and the inductance of the cable connections (figure 1).

The main goal of this work is the correlation of the impedance spectra and the capacity fading as analysed by the linear four state model [18]. This model allows us to decompose the capacity fading with the number of cycles into several well-distinguished processes. These processes can be subsequently correlated to the relaxation processes established by EIS.

Experimental

Cathode preparation and cell construction

A fraction of the EIS spectra used for this analysis was taken from a recent publication [23].
Two different types of cells were analyzed in this work. The first cells were symmetric cells consisted of two carbon electrodes separated by a Celgard® 2500 membrane. The electrodes were soaked with 14 µL of a 50 mM solution of S_8 and Li_2S_x (with x =1-8) in tetraethylene glycol dimethyl ether (TEGDME, 99.9%, Sigma-Aldrich). The preparation procedure of the S_8 and Li_2S_x solutions is described elsewhere[39]. The carbon electrodes were composed of 90 wt% of Super P conductive carbon black (99%, Alfa Aesar) and 10 wt.% of polyvinylidene fluoride (PVDF, Alfa Aesar) prepared by wet-powder spraying on Al-foil. The thickness of the carbon layer was 35 ± 2 µm.
The second type of the Li/S cells were already described elsewhere [23]. Thus, the preparation of the electrode as well as the cell assembling and electrochemical testing can be found in an earlier publication [23]. In short, the cathode consisted of 50 wt% sulfur (99.5%, Alfa Aesar), 40 wt% Super P conductive carbon black (99%, Alfa Aesar), and 10 wt% polyvinylidenefluoride (PVDF, Alfa Aesar). As electrolyte, 1M $LiPF_6$ in TEGDME and as separator, Celgard 2500 were used.

Electrochemical testing

An electrochemical workstation (Zahner® IM6 with Thales battery software) was used to carry out the electrochemical testing of the batteries. A frequency range from 1 MHz (ω_n) to 60 mHz (ω_1) and an excitation voltage of 5 mV were applied for performing the EIS measurements. The discharge/charge procedure for the Li/S cell was performed at constant current density (300 mA g_{sulfur}^{-1}, 0.18C) within voltage range 2.8–1.5 V. EIS spectra were recorded in equidistant charge intervals of 50 mC during the first cycle [23].

Data Processing

In a first step, the measured impedance spectra were corrected with the ZHIT-algorithm [40] to suppress the occurrence of artefacts that can be caused by time-dependent changes of the electrochemical system while measuring the impedance spectra.

Equivalent Circuit Model

The corrected EIS spectra were fitted with a linear equivalent circuit model (ECM) illustrated in figure 1 by using a modification of the well-known Levenberg-Marquardt algorithm (LMA). The ECM consists of four different elements in series reflecting the major processes of an electrochemical cell.

The value of R_S represents the ohmic resistance attributed to the liquid solution, collectors and cell connections. The inductance L contributes to the imaginary part of the impedance and becomes relevant at very high frequencies ω. The parameter A_W represents the ion diffusion inside an infinitely long diffusion layer (semi-infinite Warburg impedance). On a Nyquist plot the infinite Warburg impedance appears as a diagonal line with a slope of 0.5.

The superposition of RC-elements represents the distribution of relaxation times. All charge transfer reaction at the electrodes can be expressed by a parallel circuit of a double layer capacity C_{dl} and complex Faradaic impedance Z_f that represents a net current flowing through the electrode surface. This charge transfer can be decomposed by the DRT method to obtain a relaxation time spectrum $\gamma(\tau)$. This transformed view facilitates the determination and the distinction of charge transfer reactions.

Levenberg-Marquardt Algorithm

According to the ECM illustrated in figure 1 the measured impedance data $Z_{\mathrm{data}}(\omega)$ can be with $Z_{\mathrm{model}}(\omega)$.

$$Z_{\mathrm{model}}(\omega) = -\frac{A_w}{\sqrt{\omega}}(\mathrm{i}-1) + \mathrm{i}\omega L + R_S - \int \frac{\gamma(\tau)}{1+\mathrm{i}\omega\tau}\mathrm{d}\tau \quad (1)$$

The relaxation time distribution function $\gamma(\tau)$ is defined by

$$\int \gamma(\tau)\mathrm{d}\tau = \sum_{i=1}^{n} R_i \quad (2)$$

In the case of discrete data points the relaxation time distribution integral can be expressed with a matrix multiplication as follows:

$$\vec{Z}_{\mathrm{model}}(\omega) = \mathbf{Z}'(\omega\tau)\cdot\vec{\gamma} + \mathrm{i}\cdot\mathbf{Z}''(\omega\tau)\cdot\vec{\gamma} \quad (3)$$

Both matrices $\mathbf{Z}'(\omega\tau)$ and $\mathbf{Z}''(\omega\tau)$ represent the real and imaginary core of the relaxation time distribution integral (eq. 1), respectively; while $\vec{\gamma}$ is a column vector with $n-3$ entries.

$$\mathbf{Z}'(\omega\tau)_{ij} = \frac{1}{1+\left(\omega_i\tau_j\right)^2} \quad (4)$$

$$\mathbf{Z}''(\omega\tau)_{ij} = \frac{\omega_i\tau_j}{1+\left(\omega_i\tau_j\right)^2} \quad (5)$$

$$\tau_j \in \left[\underbrace{\frac{1}{\omega_n},\ldots,\frac{1}{\omega_1 10^{-2}}}_{n-3\ \text{elements}}\right] \quad (6)$$

The $n-3$ values of the relaxation time τ were calculated from the n values of the measured frequencies. For this calculation the lowest frequency ω_1 was reduced by two orders of magnitude to include also the influence of relaxation processes at very low frequencies. This procedure suppresses artefacts of the DRT-function of very slow relaxation processes that contribute to the impedance spectra with very low relaxation frequencies outside of the measured interval.

The LMA is a combination of two minimization methods: the gradient descent method and the Gauss-Newton method. Hence, the algorithm acts more like a gradient-descent method when the parameters are far from their optimal value and more like the Gauss-Newton method when the parameters are close to their optimal value. The contribution of each method to the fitting routine is controlled by the regularization parameter λ. The solution vector $\vec{\delta}$ has to be calculated in each iteration step by solving the linear equation system:

$$(\mathbf{J}^T\mathbf{J} + \lambda\cdot\mathrm{diag}(\mathbf{J}^T\mathbf{J}) + \mathbf{D})\cdot\vec{\delta} = \mathbf{J}^T\left(\left|\vec{Z}_{\mathrm{data}} - \vec{Z}_{\mathrm{model}}(\vec{\beta})\right|\right) \quad (7)$$

Here $\mathbf{J}$ is the complex Jacobi matrix that is defined with

$$\mathbf{J} = \frac{\partial\vec{Z}_{\mathrm{model}}(\vec{\beta})}{\partial\vec{\beta}} = \mathbf{J}' + \mathrm{i}\cdot\mathbf{J}'' \quad (8)$$

$$\mathbf{J}'_{ji} = \begin{cases} i = 1: -\omega_j^{-1/2} \\ i = 2: 0 \\ i = 3: 1 \\ \text{else}, \mathbf{Z}'(\omega\tau)_{ji} \end{cases} \quad (9.1) \qquad \mathbf{J}''_{ji} = \begin{cases} i = 1: -\omega_j^{-1/2} \\ i = 2: \omega_j \\ i = 3: 0 \\ \text{else}, \mathbf{Z}''(\omega\tau)_{ji} \end{cases} \quad (9.2)$$

The n-dimensional parameter vector $\vec{\beta}$ can be expressed with

$$\vec{\beta}^T = (A_W, L, R, \gamma_1, \dots, \gamma_{n-3}) \quad (10)$$

The diagonal matrix **D** serves as a weighting function to ensure good fitting with the model for very large as well as very small values of the impedance data. This matrix has only non-zero entries on its principal diagonal $\mathbf{D}_{ii} = \vec{d}$.

$$\vec{d}^T = \left(0,0,0, Z_{\text{data},1}, \dots, Z_{\text{data},n}\right) \quad (11)$$

The n-dimensional step vector $\vec{\delta}$ gives after each iteration step an adjusted parameter vector $\overrightarrow{\beta}_{\text{new}}$.

$$\vec{\beta}_{\text{new}} = \left|\vec{\beta} + \vec{\delta}\right| \quad (12)$$

All entries of the first vector $\vec{\beta}$ (starting vector) were set to one and the regularization parameter λ is set to 0.1.

Results and Discussion

Analysis of capacity fading with a linear four-state model

The electrochemical discharge and charge capacities C_{ec} were fitted with a linear four state model (eq. 13) that was published elsewhere [18].

$$C_{\text{ec}} = C_{\max} \cdot [f_{\text{fast}}(1 - k_{\text{fast}})^{nc} + f_{\text{slow}}(1 - k_{\text{slow}})^{nc}] \quad (13)$$

A fast (blue line) and a slow (green line) fading process can be identified at low and high cycle numbers, respectively (figure 2) and are in an good agreement with the EIS data, discussed in detail later. The fading process after charge possesses the lower decaying rates. The parameters resulting from the analysis of both curves are listed in table 1.

It is remarkable that already before the first charge 41% (f_{dead}) of the maximum capacity $C_{\max}$ (1675 mAh g_{sulfur}^{-1}) cannot be retained anymore. However, it is important to mention that the measurements were carried out in a non-optimized cathode, which consisted in a simple Sulfur/Carbon composite of sulfur micro-particles surrounded by Carbon Black nano-particles. In this way, the processes responsible for the capacity fading are more intensified than that for the other cell configurations with higher capacity retention. While the decay rates for the slow fading process are very similar the fast capacity decay differs by a factor of more than two.

EIS data analysis

To correlate the fading processes to electrochemical impedance spectra three experiments were performed. First, EIS was performed during the first discharge and charge in steps of 50 mC. This method resolves the intermediate states and enables the correlation of relaxation processes to the formation of SEI layers on both electrodes. Second, the analysis of symmetric cells with different polysulfide solutions gives information about the influence of the sulfur ions on the parameters A_W and R_S. Third, the evaluation of the impedance spectra of 50 cycles after discharge and after charge can be used to explain the fading curves in figure 2.

The results of the first discharge/charge cycle at different depths of discharge are illustrated in figure 3. Both voltage curves (figure 3, top) show the shape typical for Li/S cells[41]. The values of the Warburg coefficient A_W and the electrolyte solution resistance R_S (figure 3,

middle) are approximately symmetric with respect to the 100% depth of dischargeline. It is interesting that the plateaus of the voltage curve show a good correlation to the plateaus of both A_W curves. Both plateaus are characterized by the presence of S_4^{2-} and S_8^{2-} intermediate species. This correlation strongly suggests that the Warburg coefficient is mainly depending on the polysulfide concentration. The parameters R_S and A_W are defined as follows:

$$R_S \sim \frac{1}{\sum c_i z_i^2 D_i} \qquad (14.1) \qquad A_W \sim \sum \frac{1}{c_i z_i^2 \sqrt{D_i}} \qquad (14.2)$$

Here c_i, z_i and D_i are the concentration of each ion species, the valence and the diffusion constant of each ion species in the electrolyte solution. Eq. (14.1) shows that the solution resistance R_S is mainly governed by the Li^+-ion because of their higher concentration ($LiPF_6$ additive, two Li^+-ions per sulfur-ion) and high diffusion constant (small solvation shell radius). Contrary, the Warburg mass transfer coefficient is ruled by species with lower concentrations and low diffusion constants like the sulfur anions S_x^{2-} (large solvation shell radius).

The electrolyte solution resistance curves of both processes possess a maximum between the plateaus (black arrows) of the voltage profile. According to the work of Cuisinier *et al.* [42] and Cañas *et al.* [39] the maximum concentration of S_x^{2-} species is reached at these depths of discharge. The interaction of the solvent molecules with the sulfur anions leads to an increase in viscosity which in turn results in a higher solution resistance and lower A_W values. This assumption will be further substantiated by the results illustrated in figure 4 below.

The DRT spectra (figure 3, bottom) exhibit also a symmetric shape for relaxation times between 10^3 and 10^{-1} seconds. Very high values of $\gamma(\tau)$ can be found at high relaxation times and at 0% and 100% depth of discharge. This high impedance phase vanishes and reappears at the ends of the discharge and charge process. Other investigations with X-ray diffraction [13,32,43] and X-ray absorption spectroscopy [13,44] have already intensively investigated the formation processes of the solid sulfur phases. These investigations strongly substantiate the assumption that this slow relaxation process can be assigned to the two solid sulfur phases S_8 and Li_2S. The part of the DRT spectra at relaxation times lower than 10^{-1} s show an asymmetric distribution indicating a non-reversible process for these τs at around 10^{-3} s. This relaxation process does not significantly change for varying depths of discharge. It is assumed that this process arises from the lithium anode. This assumption is supported by the results of Aurbach *et al.* [11,45] who detected also for various organic solvents a SEI layer related relaxation process at the lithium anode at around 1 kHz ($\tau = 10^{-3}$ s).
In general, every deviation from a symmetric distribution indicates non-reversible processes implying the occurrence of parasitic side reactions in the system which in turn leads to capacity fading.

Figure 4 illustrates the results of the symmetric cell experiments. The solutions termed Li_2S_2…Li_2S_8 do not consist of isolated polysulfides but rather a distribution of Li_2S_x (x=1…8), which lead to different average of polysulfide lengths. The curve of the electrolyte solution resistance exhibit low values of R_S for intermediates Li_2S_2, Li_2S and S_8 indicating the expected weak solvation of these hardly soluble solutes. All other polysulfide species have a high solution resistance which can be explained by the increase in dynamic viscosity of the electrolyte solution and respective decreased values of the A_W (see eq. 14.2). Recent publications discuss the formation of large polysulfide clusters due to binding energy minimization [46,47]. This would support the above explanation by an increase in viscosity. Furthermore, these publications predict an enhanced clustering for Li_2S_4, Li_2S_6 and Li_2S_8 which is confirmed by elevated values of R_S for these types of polysulfides. The progress of the Warburg coefficient (figure 4, top) is very similar to that in figure 3 during charge which is

consistent with the expected occurrence of sulfur intermediates in this electrochemical multi-step process.

The DRT spectra in figure 4 show some similarities to the charging DRT spectra in figure 3. High values of $\gamma(\tau)$ are obtained for the Li_2S and S_8 phase at large relaxation times τ. Also, the gap at 10^1 s can be found in the discharge spectra. This indicates that slow relaxation processes in Li/S cells can be assigned to the sulfur redox processes.
Figure 5 and 6 illustrates the analysis of the impedance over 50 cycles after discharge and charge, respectively.

The DRT spectra (figure 5 and 6) represent the starting situation of the subsequent charge or discharge step. This means that the discharge and charge capacity C_{ec} (figure 2) are influenced by the SEI layers formed in the prior charge or discharge step, respectively. The black lines in the DRT spectra mark the cycle number where the contribution of the fast fading process is less than 0.5%. For higher cycle numbers, the relaxation processes at τs lower than 10^{-1} s maintain almost constant and are well-defined (6 traces can be observed at low relaxation times). As mentioned above, this process is assigned to charge transfer reactions at the lithium anode. Lu *et al.*[48] demonstrated using cross-sectional images of the rapidly formation of a highly resistive solid electrolyte interphase which grows on the Li side. Our measurements were carried out at relative low C-rates (0.18C); thus, we can assume that the fast capacity fading during the first cycles in Li/S cells is caused by the relaxation processes at the lithium anode. Furthermore, at low C-rate the formation of a stable SEI layer may explain the constant charge transfer resistance after several cycles. At higher C-rates, this SEI layer may not be stable.
The rate of the fast capacity decay process was calculated to be around two times higher for the discharge process than for the charge process. This may be explained by the formation of Li_2S at the end of discharge, which can build up isolating layers/regions on the anode surface. On contrary, the solid charge product sulfur is more soluble in the electrolyte. Thus, the formation of isolating layer on the anode surface is less probable.
The processes occurring at long relaxation times, namely charge transfer processes and formation of solid products at/on the cathode have the highest resistance contribution, as already stated in a previous publication [23]. Progressive changes in the morphology of the cathode structure due to dissolution and crystallization processes of active solid phases may be an important contribution on the low capacity fading.
The Warburg coefficient values after charge (figure 6, top) decreases in the first cycles and then rises again to almost stable values. According to equation 14.2 this reflects an increase of the concentration of long chain polysulfides (Li_2S_8) followed by a decrease in polysulfide order. The curve flattens after the contribution of the fast relaxation process vanishes (black line). From this cycle on the system stabilizes. The other characteristic curves are nearly constant for all cycle numbers.

The DRT analysis is clearly advantageous because it can distinguish between different relaxation processes. Therefore it is possible to show the Nyquist plots of only fast relaxation process that occur at the anode (figure 7).

Figure 7 serves as a comparison between DRT and Nyquist representation. Both Nyquist plots reflect the change of charge transfer processes with cycle number. Nevertheless the superposition of six semi circles is difficult to observe in this representation form. It is interesting to note that similar processes have already been postulated by Aurbach *et al.* [34,35,45]. In their work lithium metal electrodes were exposed to different electrolytes and a layered structure at the anode fitted by a series of RC-units has been suggested. This serial circuit of six elements is reflected by the occurrence of six processes in the DRT spectra after discharge (figure 5) and after charge (figure 6). These processes are observed in the bottom of the figures in the range of $\tau = 10^{-1}$–10^{-6}s as blue/green traces.

Conclusion

In this work, the capacity fading of Li/S battery was studied by electrochemical impedance spectroscopy for over 50 cycles. We propose an equivalent circuit with four elements and the use of the Levenberg-Marquardt algorithm as effective method to analyze the relaxation processes in Li/S batteries. This distribution of relaxation time (DRT) method leads the distinction of the charge transfer processes at the lithium anode and the sulfur cathode. Furthermore, the analysis of the capacity fading curve with a linear four-state model revealed a fast and a slow capacity fading processes. The fast capacity fading process, responsible for the high capacity decay in the first cycles, was correlated to relaxation processes occurring at the lithium anode. This is related to a formation of a resistive SEI on the anode. This finding underscores the important role of anodic processes for capacity fading in Li/S-cells.

Acknowledgement

We thank Sijie Zhao for helping with the EIS measurements of the symmetric cells. E.Härk is grateful for funding from the Estonian centre of excellence in science project TK117T “High-technology materials for sustainable development".

Literature

[1] A. Manthiram, Y. Fu, S.-H. Chung, C. Zu, Y.-S. Su, Rechargeable Lithium–Sulfur Batteries, Chem. Rev. 114 (2014) 11751–11787. doi:10.1021/cr500062v.

[2] P.G. Bruce, S. a. Freunberger, L.J. Hardwick, J.-M. Tarascon, Li–O2 and Li–S batteries with high energy storage, Nat. Mater. 11 (2011) 172–172. doi:10.1038/nmat3237.

[3] D. Bresser, S. Passerini, B. Scrosati, Recent progress and remaining challenges in sulfur-based lithium secondary batteries - A review., Chem. Commun. 49 (2013) 10545–62. doi:10.1039/c3cc46131a.

[4] A. Rosenman, E. Markevich, G. Salitra, D. Aurbach, A. Garsuch, F.F. Chesneau, Review on Li-Sulfur Battery Systems: an Integral Perspective, Adv. Energy Mater. 5 (2015) 1500212. doi:10.1002/aenm.201500212.

[5] Z. Deng, Z. Zhang, Y. Lai, J. Liu, J. Li, Y. Liu, Electrochemical Impedance Spectroscopy Study of a Lithium/Sulfur Battery: Modeling and Analysis of Capacity Fading, J. Electrochem. Soc. 160 (2013) A553–A558. doi:10.1149/2.026304jes.

[6] H. Yao, G. Zheng, P.-C. Hsu, D. Kong, J.J. Cha, W. Li, et al., Improving lithium-sulphur batteries through spatial control of sulphur species deposition on a hybrid electrode surface., Nat. Commun. 5 (2014) 3943. doi:10.1038/ncomms4943.

[7] X. Ji, S. Evers, R. Black, L.F. Nazar, Stabilizing lithium-sulphur cathodes using polysulphide reservoirs., Nat. Commun. 2 (2011) 325. doi:10.1038/ncomms1293.

[8] Y. V. Mikhaylik, J.R. Akridge, Polysulfide Shuttle Study in the Li/S Battery System, J. Electrochem. Soc. 151 (2004) A1969. doi:10.1149/1.1806394.

[9] J.H. Shin, E.J. Cairns, Characterization of N-Methyl-N-Butylpyrrolidinium Bis(trifluoromethanesulfonyl)imide-LiTFSI-Tetra(ethylene glycol) Dimethyl Ether Mixtures as a Li Metal Cell Electrolyte, J. Electrochem. Soc. 155 (2008) A368. doi:10.1149/1.2869876.

[10] Z. Li, J. Huang, B. Yann Liaw, V. Metzler, J. Zhang, A review of lithium deposition in lithium-ion and lithium metal secondary batteries, J. Power Sources. 254 (2014) 168–182. doi:10.1016/j.jpowsour.2013.12.099.

[11] D. Aurbach, E. Pollak, R. Elazari, G. Salitra, C.S. Kelley, J. Affinito, On the Surface Chemical Aspects of Very High Energy Density, Rechargeable Li–Sulfur Batteries, J. Electrochem. Soc. 156 (2009) A694. doi:10.1149/1.3148721.

[12] M.A. Lowe, J. Gao, H.D. Abruña, Mechanistic insights into operational lithium–sulfur batteries by in situ X-ray diffraction and absorption spectroscopy, RSC Adv. 4 (2014) 18347. doi:10.1039/c4ra01388c.

[13] S. Waluś, C. Barchasz, J.-F. Colin, J.-F. Martin, E. Elkaïm, J.-C. Leprêtre, et al., New insight into the working mechanism of lithium-sulfur batteries: in situ and operando X-ray diffraction characterization., Chem. Commun. 49 (2013) 7899–901. doi:10.1039/c3cc43766c.

[14] R. Xu, I. Belharouak, X. Zhang, R. Chamoun, C. Yu, Y. Ren, et al., Insight into Sulfur Reactions in Li–S

Batteries, ACS Appl. Mater. Interfaces. 6 (2014) 21938–21945. doi:10.1021/am504763p.

[15] D.N. Fronczek, W.G. Bessler, Insight into lithium-sulfur batteries: Elementary kinetic modeling and impedance simulation, J. Power Sources. 244 (2013) 183–188. doi:10.1016/j.jpowsour.2013.02.018.

[16] C.P. Yang, Y.X. Yin, H. Ye, K.C. Jiang, J. Zhang, Y.G. Guo, Insight into the effect of boron doping on sulfur/carbon cathode in lithium-sulfur batteries, ACS Appl. Mater. Interfaces. 6 (2014) 8789–8795. doi:10.1021/am501627f.

[17] L. Yuan, X. Qiu, L. Chen, W. Zhu, New insight into the discharge process of sulfur cathode by electrochemical impedance spectroscopy, J. Power Sources. 189 (2009) 127–132. doi:10.1016/j.jpowsour.2008.10.033.

[18] S. Risse, S. Angioletti-Uberti, J. Dzubiella, M. Ballauff, Capacity fading in lithium/sulfur batteries: A linear four-state model, J. Power Sources. 267 (2014) 648–654.

[19] M.B. Pinson, M.Z. Bazant, Theory of SEI Formation in Rechargeable Batteries: Capacity Fade, Accelerated Aging and Lifetime Prediction, J. Electrochem. Soc. 160 (2012) A243–A250. doi:10.1149/2.044302jes.

[20] J. Zheng, M. Gu, H. Chen, P. Meduri, M.H. Engelhard, J.-G. Zhang, et al., Ionic liquid-enhanced solid state electrolyte interface (SEI) for lithium–sulfur batteries, J. Mater. Chem. A. 1 (2013) 8464. doi:10.1039/c3ta11553d.

[21] M. Itagaki, N. Kobari, S. Yotsuda, K. Watanabe, S. Kinoshita, M. Ue, In situ electrochemical impedance spectroscopy to investigate negative electrode of lithium-ion rechargeable batteries, J. Power Sources. 135 (2004) 255–261. doi:10.1016/j.jpowsour.2004.04.004.

[22] S. Cheng, J. Zhang, M. Zhao, C. Cao, Electrochemical impedance spectroscopy study of Ni/MH batteries, J. Alloys Compd. 293 (1999) 814–820. doi:10.1016/S0925-8388(99)00363-1.

[23] N.A. Cañas, K. Hirose, B. Pascucci, N. Wagner, K.A. Friedrich, R. Hiesgen, Investigations of lithium-sulfur batteries using electrochemical impedance spectroscopy, Electrochim. Acta. 97 (2013) 42–51. doi:10.1016/j.electacta.2013.02.101.

[24] H. Schichlein, A.C. Müller, M. Voigts, A. Krügel, E. Ivers-Tiffeé, Deconvolution of electrochemical impedance spectra for the identification of electrode reaction mechanisms in solid oxide fuel cells, J. Appl. Electrochem. 32 (2002) 875–882. doi:10.1023/A:1020599525160.

[25] J. Illig, M. Ender, T. Chrobak, J.P. Schmidt, D. Klotz, E. Ivers-Tiffee, Separation of Charge Transfer and Contact Resistance in LiFePO4-Cathodes by Impedance Modeling, J. Electrochem. Soc. 159 (2012) A952–A960. doi:10.1149/2.030207jes.

[26] P. Verma, P. Maire, P. Novák, A review of the features and analyses of the solid electrolyte interphase in Li-ion batteries, Electrochim. Acta. 55 (2010) 6332–6341. doi:10.1016/j.electacta.2010.05.072.

[27] J. Zheng, J. Tian, D. Wu, M. Gu, W. Xu, C. Wang, et al., Lewis Acid–Base Interactions between Polysulfides and Metal Organic Framework in Lithium Sulfur Batteries, Nano Lett. 14 (2014) 2345–2352. doi:10.1021/nl404721h.

[28] Y. Yang, G. Zheng, Y. Cui, A membrane-free lithium/polysulfide semi-liquid battery for large-scale energy storage, Energy Environ. Sci. 6 (2013) 1552–1558. doi:10.1039/C3EE00072A.

[29] A. Lasia, Electrochemical Impedance Spectroscopy and its Applications, in: Mod. Asp. Electrochem., Kluwer Academic Publishers, Boston, 2002: pp. 143–248. doi:10.1007/0-306-46916-2_2.

[30] G. Láng, K.E. Heusler, Remarks on the energetics of interfaces exhibiting constant phase element behaviour, J. Electroanal. Chem. 457 (1998) 257–260. doi:10.1016/S0022-0728(98)00301-5.

[31] M.R. Shoar Abouzari, F. Berkemeier, G. Schmitz, D. Wilmer, On the physical interpretation of constant phase elements, Solid State Ionics. 180 (2009) 922–927. doi:10.1016/j.ssi.2009.04.002.

[32] L. Yuan, X. Qiu, L. Chen, W. Zhu, New insight into the discharge process of sulfur cathode by electrochemical impedance spectroscopy, J. Power Sources. 189 (2009) 127–132. doi:10.1016/j.jpowsour.2008.10.033.

[33] S. Xiong, K. Xie, Y. Diao, X. Hong, On the role of polysulfides for a stable solid electrolyte interphase on the lithium anode cycled in lithium-sulfur batteries, J. Power Sources. 236 (2013) 181–187. doi:10.1016/j.jpowsour.2013.02.072.

[34] D. Aurbach, A. Zaban, Impedance spectroscope of lithium electrodes Part 2. The behaviour in propylene carbonate solutions — the significance of the data obtained, J. Electroanal. Chem. 367 (1994) 15–25. doi:10.1016/0022-0728(93)02998-W.

[35] D. Aurbach, A. Zaban, Impedance spectroscopy of lithium electrodes: Part 1. General behavior in propylene carbonate solutions and the correlation to surface chemistry and cycling efficiency, J. Electroanal. Chem. 348 (1993) 155–179. doi:10.1016/0022-0728(93)80129-6.

[36] P. Büschel, U. Tröltzsch, O. Kanoun, Calculation of the distribution of relaxation times for characterization

of the dynamic battery behavior, Int. Multi-Conference Syst. Signals Devices, SSD 2012 - Summ. Proc. (2012) 9–11. doi:10.1109/SSD.2012.6198129.

[37] J. Macutkevic, J. Banys, a Matulis, Determination of the Distribution of the Relaxation Times from Dielectric Spectra, Nonlinear Anal. Model. Control. 9 (2004) 75–88.

[38] J.J. More, The Levenberg-Marquardt algorithm: Implementation and theory, Lect. Notes Math. 630 (1978) 105–116. doi:10.1007/BFb0067700.

[39] N.A. Cañas, D.N. Fronczek, N. Wagner, A. Latz, K.A. Friedrich, Experimental and Theoretical Analysis of Products and Reaction Intermediates of Lithium–Sulfur Batteries, J. Phys. Chem. C. 118 (2014) 12106–12114. doi:10.1021/jp5013208.

[40] C.A. Schiller, F. Richter, E. Gülzow, N. Wagner, Validation and evaluation of electrochemical impedance spectra of systems with states that change with time, Phys. Chem. Chem. Phys. 3 (2001) 374–378. doi:10.1039/b007678n.

[41] S.S. Zhang, Liquid electrolyte lithium/sulfur battery: Fundamental chemistry, problems, and solutions, J. Power Sources. 231 (2013) 153–162. doi:10.1016/j.jpowsour.2012.12.102.

[42] M. Cuisinier, P.E. Cabelguen, S. Evers, G. He, M. Kolbeck, A. Garsuch, et al., Sulfur speciation in Li-S batteries determined by operando X-ray absorption spectroscopy, J. Phys. Chem. Lett. 4 (2013) 3227–3232. doi:10.1021/jz401763d.

[43] N. a. Cañas, S. Wolf, N. Wagner, K.A. Friedrich, In-situ X-ray diffraction studies of lithium-sulfur batteries, J. Power Sources. 226 (2013) 313–319. doi:10.1016/j.jpowsour.2012.10.092.

[44] M.U.M. Patel, I. Arčon, G. Aquilanti, L. Stievano, G. Mali, R. Dominko, X-ray Absorption Near-Edge Structure and Nuclear Magnetic Resonance Study of the Lithium-Sulfur Battery and its Components, ChemPhysChem. 15 (2014) 894–904. doi:10.1002/cphc.201300972.

[45] A. Zaban, E. Zinigrad, D. Aurbach, Impedance Spectroscopy of Li Electrodes. 4. A General Simple Model of the Li–Solution Interphase in Polar Aprotic Systems, J. Phys. Chem. 100 (1996) 3089–3101. doi:10.1021/jp9514279.

[46] B. Wang, S.M. Alhassan, S.T. Pantelides, Formation of Large Polysulfide Complexes during the Lithium-Sulfur Battery Discharge, Phys. Rev. Appl. 2 (2014) 1–7. doi:10.1103/PhysRevApplied.2.034004.

[47] M. Vijayakumar, N. Govind, E. Walter, S.D. Burton, A. Shukla, A. Devaraj, et al., Molecular structure and stability of dissolved lithium polysulfide species., Phys. Chem. Chem. Phys. 16 (2014) 10923–32. doi:10.1039/c4cp00889h.

[48] D. Lu, Y. Shao, T. Lozano, W.D. Bennett, G.L. Graff, B. Polzin, et al., Failure Mechanism for Fast-Charged Lithium Metal Batteries with Liquid Electrolytes, Adv. Energy Mater. 5 (2015). doi:10.1002/aenm.201400993.

List of Tables

Table 1: Summary of fit parameters and errors extracted from the capacity fading curves of figure 2. f_{dead} is defined by $1 - f_{\mathrm{fast}} - f_{\mathrm{slow}}$ and represents the initially inactive phase.

	discharge	**charge**
f_{fast}	0.42 ± 0.024	0.22 ± 0.013
f_{slow}	0.44 ± 0.007	0.37 ± 0.014
f_{dead}	0.14 ± 0.032	0.41 ± 0.027
k_{fast}	0.38 ± 0.026	0.16 ± 0.019
k_{slow}	0.028 ± 0.0007	0.023 ± 0.0011

Figures

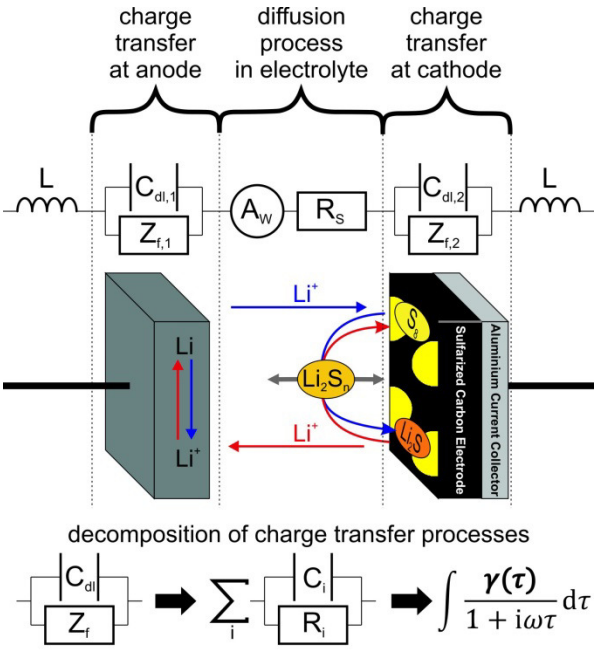

Figure 1: Equivalent circuit model for the fitting of impedance data. The two charge transfer processes at the lithium anode (1) sulfur cathode (2) and are represented by a parallel circuit of a Faradaic impedance Z_f and a double layer capacity C_{dl} [29]. These processes can be decomposed with a series of RC-units (bottom) to obtain the distribution of relaxation times $\gamma(\tau)$.The R_is and C_is are the resistances and capacities, respectively, of the Debye relaxations used for the decomposition method. The diffusion processes in the electrolyte are simulated with a Warburg impedance A_W and a solution resistance R_S.

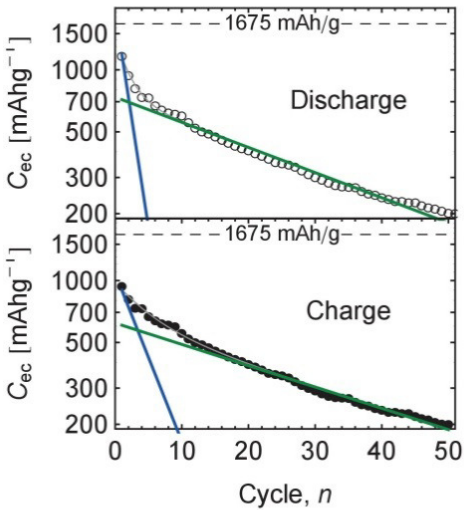

Figure 2: Capacity fading curves after discharge (top) and after charge (bottom). The blue line and the green line mark the influence of the fast and slow capacity fading process, respectively.

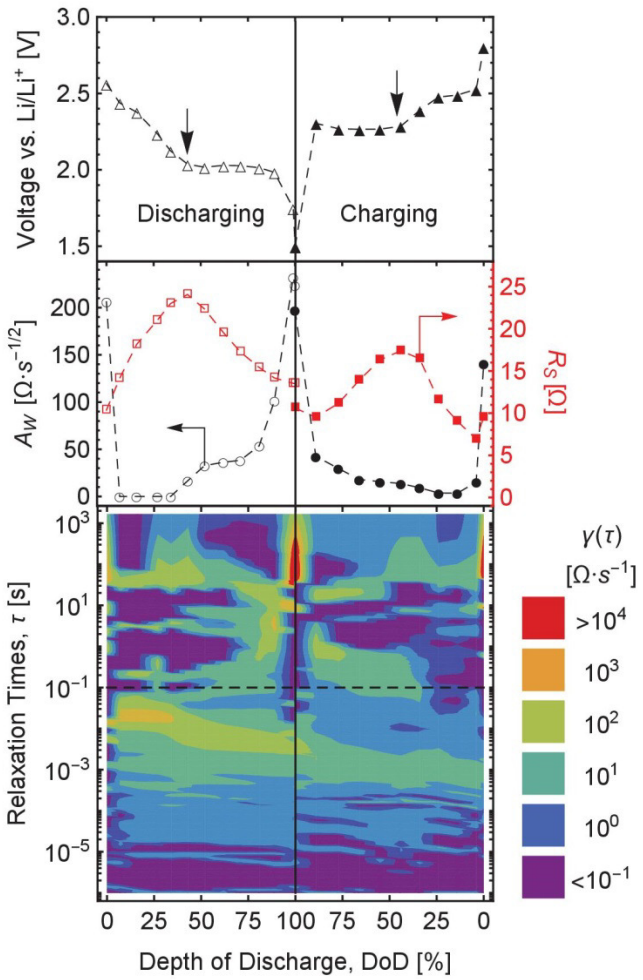

Figure 3: Voltage curve (top), Warburg coefficient and electrolyte solution resistance (middle) and contour plot of the calculated DRT function during first discharge and subsequent first charge at different depths of discharge.

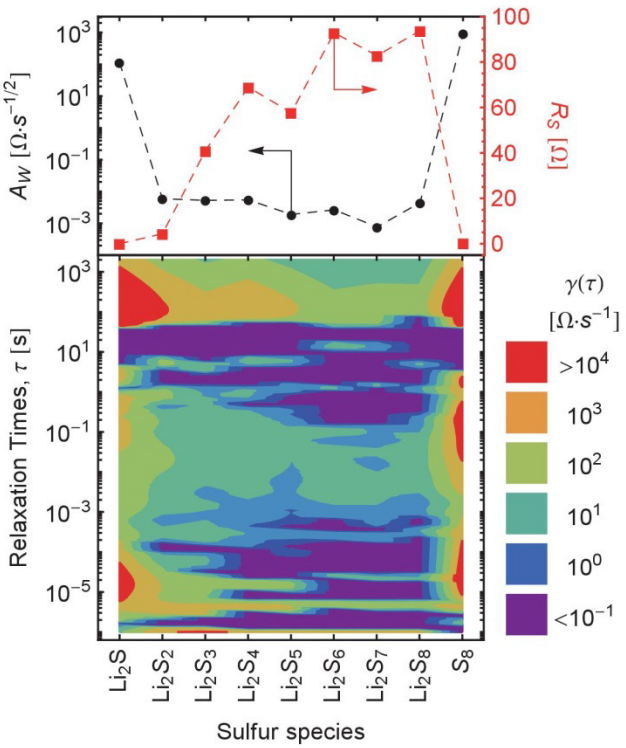

Figure 4: Warburg coefficient and solution resistance (top) and contour plot of the calculated DRT function for solutions of different sulfur species with a concentration of 50 mM.

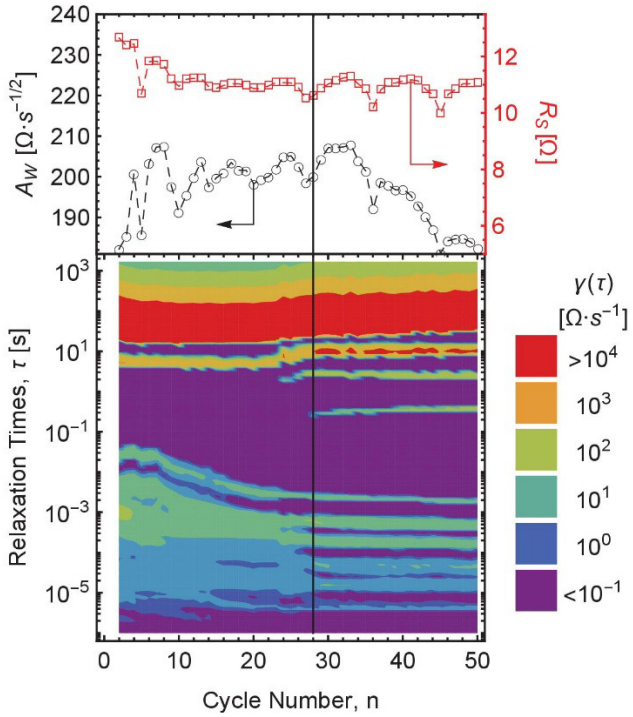

Figure 5: Cycle dependent EIS results after discharge. Solution resistances R_S (red) and Warburg coefficient A_W (black) are shown in the top row. The calculated DRT spectra are shown at the bottom. The black line indicates the cycle number where the contribution of the fast charge capacity fading process is less than 0.5%.

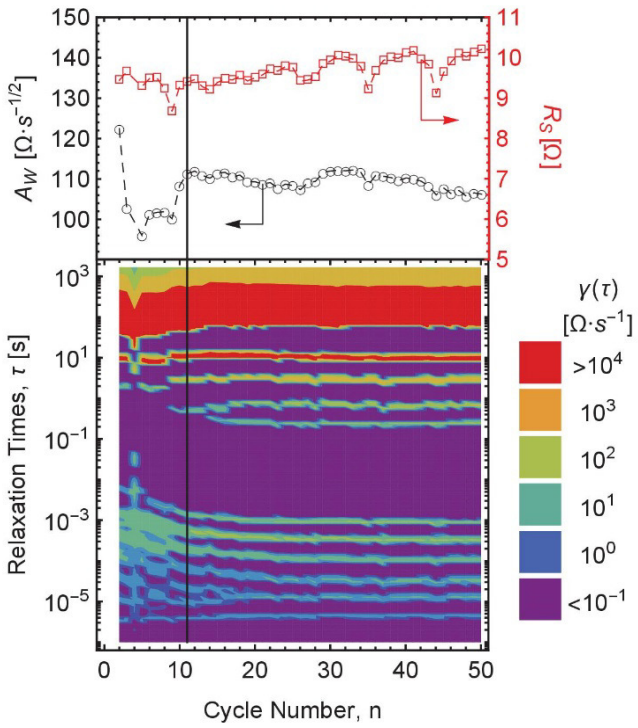

Figure 6: Cycle dependent EIS results after charge. Solution resistances R_S (red) and Warburg coefficient A_W (black) are shown in the top row. The calculated DRT spectra are shown at the bottom. The black line indicates the cycle number where the contribution of the fast charge capacity fading process is less than 0.5%.

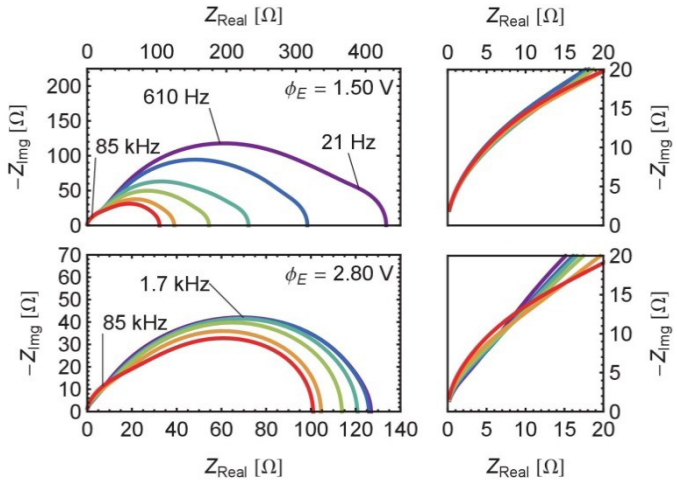

Figure 7: Nyquist plots of processes at lithium anode after discharge (top) and after charge (bottom) of the 1st (purple), 2nd (blue), 5th (turquoise), 10th (green), 20th (orange) and 50th (red) cycle. The curves of the 1st and 2nd cycle after charge (bottom) are overlapping each other. The maximum impedance values decreases with cycle number.